Quantification of mixture composition, liquid-phase fraction and - temperature in transcritical sprays

Tobias C. Klima [a,c], Andreas Peter [b], Sebastian Riess [b,c], Michael Wensing [b,c], Andreas S. Braeuer [a,d,*]

[a] Institute of Thermal-, Environmental-, and Resources' Process Engineering (ITUN), Technische Universität Bergakademie Freiberg (TUBAF), Germany
[b] Institute of Engineering Thermodynamics (LTT), Friedrich-Alexander-Universität Erlangen-Nürnberg (FAU), Germany
[c] Erlangen Graduate School in Advanced Optical Technologies (SAOT), Friedrich-Alexander-Universität Erlangen-Nürnberg (FAU), Germany
[d] Zentrum für effiziente Hochtemperatur-Stoffwandlung (ZeHS), Technische Universität Bergakademie Freiberg (TUBAF), Freiberg, Germany

HIGHLIGHTS

- New measurement approach for liquid phase fractions and liquid phase temperatures.
- Data from measurements in sprays at IC-engine conditions.
- Identification of liquid phase at supercritical conditions does not rely on visibility of phase boundaries.

GRAPHICAL ABSTRACT
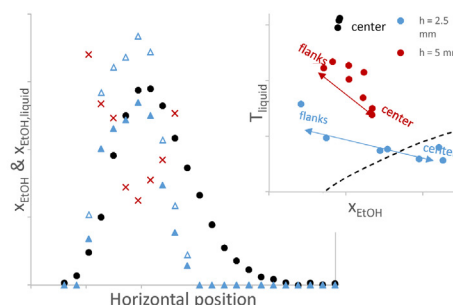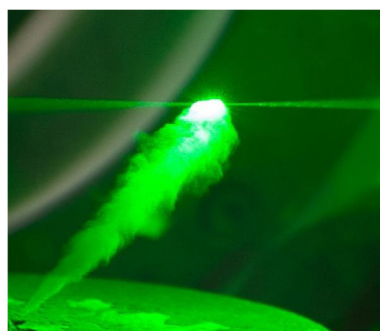
ARTICLE INFO

ABSTRACT

How do fuel and air mix, if a liquid fuel is injected into an environment featuring pressure and temperature that exceed the critical pressure and the critical temperature of the fuel? It is subject of current discussion on whether and if so when, the fuel/air-mixture becomes supercritical or not. We here report experimental data comprising three mixture properties that are relevant for the current debate, all spatially and temporally resolved throughout the spray and injection event: The overall composition of the fuel/air-mixture, the liquid fraction of the fuel/air-mixture, and the temperature of the liquid phase. To this end, we applied Raman spectroscopy and gave special attention to the signature of the Raman OH-band of ethanol, which we used as fuel. Its signature is connected to the development of a hydrogen bonded network between the ethanol molecules and thus extremely sensitive to thermodynamic state and temperature. Measurements were carried out in a high-pressure, high-temperature combustion vessel in a pressure range of 3−8 MPa and a temperature range of 573−923 K. For the highest set temperature we found ethanol in liquid-like mixtures that exceeded the mixture critical temperature. This is an indication of the existence of a single-phase mixing path.

* Corresponding author.
    E-mail address: andreas.braeuer@tu-freiberg.de (A.S. Braeuer).

1. Introduction

In modern energy conversion systems many processes involve the injection of a liquid fuel into an environment at elevated temperatures and pressures. Before the injection event, the fuel usually can be assigned to the liquid state, while the environment is either gaseous or supercritical. For long times after injection, when the mixing process between fuel and environment is completed, the formed mixture can clearly be assigned to a certain state of phase. Unfortunately, this is not straight forward for the instants between the start of the injection event and the completion of the mixture formation. It is intensively discussed in literature how a fuel that is injected as a liquid transits to a supercritical mixture. This transition we refer to as transcritical mixing. On its way to the supercritical mixture the system may pass the two-phase (liquid-gas) region or alternatively circumvent it and remain in a single-phase region. Thus there is ongoing discussion in literature on when the classic two-phase theory is no longer sufficient to describe the heat and mass transfer processes governing the mixture formation. Numerous groups have tried to shed light on the matter by applying optical methods [1–8].

An extensive theoretical framework covering the transition from evaporation-driven, two-phase mixture formation to dense-fluid single-phase mixing at engine-relevant conditions was proposed by Dahms et al. [6,9,10]. Following their model, there exists a certain temperature-pressure regime where classic two-phase mixing across a clear interface between liquid and gas becomes continuous mixing across a broad diffusive mixing layer. In contrast to Dahms et al., Qiu et al. [4,11] introduced a different approach to determine the adiabatic mixing temperature. Based on their theoretical works involving phase stability analysis, they expect to find well defined liquid/gas-interfaces even at many conditions that are supercritical with respect to the pure fuel properties.

Of the numerous recent experimental works on potentially transcritical mixing processes, many have tried to detect structures indicating interfaces or their lack by imaging the spray or the jet. Manin et al. [8] reported images of single fluid elements formed during the injector closing event of an n-dodecane injection at engine-relevant conditions. They identified pressure-temperature regions where effects attributable to interface were clearly identifiable, while at higher pressures these effects appeared to be less evident. They also addressed a recurring problem when imaging at high pressure conditions: Fluctuations of the index of refraction in these compressed systems rendering clear images of the spray/jet challenging. In order to overcome imaging distortions, Falgout et al. [5] applied ballistic imaging. They detected Schlieren-like structures on the flanks of the fuel stream at pressures exceeding the critical parameter of the respective fuels and also reported that real Diesel fuel seems to fully exhibit these structures only at even higher pressures than they investigated. Furthermore, Falgout and co-workers pointed out that images do not yield information on the transcritical mixing process, and suggested Raman spectroscopic measurements. Another microscopic imaging approach by Crua et al. [7] investigated the morphological distortion of droplets as a measure of interfacial forces during transcritical mixing. They observed classical evaporation even at conditions exceeding the critical parameters of the fuel, identified a transitional mixing regime with diminished but still observable interfaces and found evidence for diffusive mixing at around 8 MPa and 1100 K. Crua and co-workers pointed out the need for quantitative temperature measurements, as only this information together with composition can truly help describe the real transcritical mixing path.

When it comes to measuring the liquid phase temperature in a spray at these conditions, remote *in-situ* techniques are required to not disturb the hydrodynamics of the process. This calls for
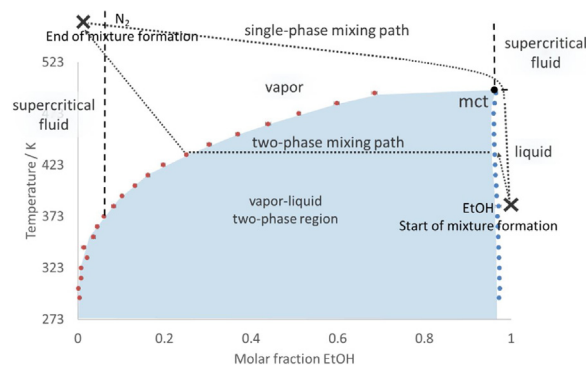

Fig. 1. Schematic mixture formation pathways in a temperature composition (Tx) diagram. Classical, evaporative mixture formation crosses the two-phase region, while single-phase mixture formation circumvents the two-phase region by passing the supercritical region.

optical techniques, and especially tracer-free ones to not alter thermodynamics of the system. We apply Raman spectroscopy spatially resolved along a line and scanned across the spray, and will show in this work how to extract information on the composition in the spray, the fraction of fuel with liquid-like properties and the temperature of the liquid-like mixture fraction from the acquired spectra. Our technique exploits the Raman signal from the CH stretching vibration (mixture composition) as well as the OH stretching vibrations (liquid phase fraction and temperature) of ethanol. Using ethanol as a surrogate, although it not being a diesel fuel, is acceptable since the physical mixture formation has been shown to be independent of the fuel and as this combination of properties is only measurable when using alcohols as fuel surrogates [12]. The stretching vibration of the OH bond of gaseous ethanol (no hydrogen bonds) exhibits a sharp peak at a Raman-shift of $3680\,cm^{-1}$, while liquid ethanol (hydrogen bonds) exhibits a broad Raman band at Raman-shifts between 3200 and $3700\,cm^{-1}$. We refer to this band as the Raman OH-band. This signal is only present in the liquid phase, and thus allows for discrimination between vapor and liquid phase [13]. Additionally, this Raman OH-band is highly sensitive to liquid-phase temperature [14]. Measurements of fuel fraction at engine conditions have been carried out before [15], and also liquid-phase temperature measurement in sprays by Raman spectroscopy exploiting the Raman OH-band are known at easier accessible conditions [16,17]. Using Raman spectroscopy to probe mixture segregation at supercritical conditions with the same approach has been carried out by Bassing et al. [18]. We here report on measurements providing all this information simultaneously at engine-relevant conditions.

2. Thermodynamic considerations

Potential transcritical mixture formation pathways between nitrogen, which is a substitute for air, and ethanol, which here is a substitute for the fuel, are schematically shown in a temperature composition (Tx) diagram in Fig. 1. We chose a Tx diagram, as the mixing process can be considered to be isobaric taking place at the set pressure. The vapor-liquid equilibrium lines are taken from our previous work on the system ethanol/nitrogen for 8 MPa [13]. The two crosses represent the states (composition and temperature) of the nitrogen and the fuel before the mixing process is initiated by injection of the fuel. The fuel is assumed to adapt to the pressure of the chamber as soon as it is has left the injection nozzle. One mixing path crosses the vapor-liquid equilibrium two-phase region, one circumvents it. Therefore, we refer to the first one as a two-phase mixing path and to the second one as a single-phase mixing path. Along the two-phase mixing path, the heat and mass

transport has to cross the phase boundary that separates the liquid fuel-rich phase from the gaseous nitrogen-rich phase. As nitrogen is provided in huge excess, the final mixture is mainly composed of nitrogen and will accommodate to the nitrogen temperature and thus is presented by the cross that also represents the nitrogen before mixing.

On the contrary, especially when after injection the heat transfer into the ethanol-rich volumes dominates over the mass transfer, the mixing path, starting from the "start of mixture formation" in Fig. 1 circumvents the vapor-liquid equilibrium region above its critical temperature and thus takes place completely in a single-phase. Therefore, the involved heat and mass transfer processes are not confronted by interfaces. Then mixing would be governed by aerodynamics and diffusion.

In the context of Fig. 1, the two example mixing paths were described referring to a Tx-diagram, which provides vapor-liquid equilibrium data for a system in thermodynamic equilibrium. But mixing processes are far from thermodynamic equilibrium and thus their interpretation based on Tx-diagrams can only provide an orientation. Within this study we aim at finding out under which conditions the mixing process follows which mixing path or maybe when the two mixing paths merge. In order to being able to do this, experimental measurement data are required that allow following the real mixing path in a Tx-diagram. Therefore we provide measurement data on the overall composition of the mixture, on the temperature of the ethanol in a liquid-like state and on the fraction of ethanol in a liquid-like state.

3. Experimental setup and data processing

A schematic overview of the experimental setup, also showing the optical pathways, is shown in Fig. 2. It is mainly composed of the high temperature and high pressure injection and combustion chamber and the optical Raman spectroscopic setup. The chamber is permanently scavenged with heated nitrogen and can be operated at up to 1000 K temperature and 10 MPa pressure. The injector has a special nozzle with three nozzle holes to allow for optical access to a single, isolated fuel stream (45° elevation angle, nozzle holes set 120° apart, see Fig. 3). The attached common rail system provides injection pressures up to 250 MPa, and the nozzle tip can be temperature controlled between 243 K and 373 K. Thus the fuel (ethanol) is definitely injected as a liquid. To ensure that each injection event is unaffected by previous ones, the injection repetition rate was set to 1 Hz. The vessel and its peripheral components are described in detail in [12], where also further information on the generated sprays can be found. A CAD sectional image of the chamber is shown in Figure SI 1 of the supplementary information (SI).

A multidimensional variation of parameters was investigated in this study. The ambient pressure p_a (where ambient refers to the inside of the chamber), the ambient temperature T_a, height above the injector h and the time after visible start of injection t_{avsoi} were varied according to Table 1. The injection pressure p_i and the fuel temperature T_f prior to injection were set to 120 MPa and 363 K, respectively.

An Agilite laser system ($E_{pulse} = 300\,mJ$, $t_{pulse} = 1\,\mu s$, $\lambda = 532\,nm$, $f = 5\,Hz$) is used for excitation of the Raman signal. The power of the pulse is low enough to prevent optical breakdown and stimulated Raman scattering. The laser beam is guided to the chamber and focused by a 2″, 300 mm focal length lens to form a beam waist in the desired measurement volume. The beam waist is imaged under 90° with a 3″ lens system (250 mm focal length on chamber side, 300 mm on spectrograph side, razor edge filter to block elastically scattered light) onto the entrance slit of an Andor Shamrock 303i imaging spectrograph equipped with

Table 1
Set of operational parameters.

p_a (MPa)	T_a (K)	h (mm)	t_{avsoi} (μs)
3	573	2.5, 5, 10	25 - 1600
	623		
	923	2.5, 5, 7.5, 10	25 - 1000
5	573	2.5, 5, 10	25 - 1600
	623		
	923	2.5, 5, 7.5, 10	25 - 1000
6	573	2.5, 5, 10	25 - 1600
	623		
	923	2.5, 5, 7.5, 10	25 - 1000
6.5	573	2.5, 5, 10	25 - 1600
	623		
	923	2.5, 5, 7.5, 10	25 - 1000
8	573	2.5, 5, 10	25 - 1600
	623		
	923	2.5, 5, 7.5, 10	25 - 1000

a 300 l/mm grating. Here, the spectrally dispersed and spatially resolved signal is detected by an Andor Newton 971 EMCCD camera (1600×400 pixels, $16\,\mu m \times 16\,\mu m$ each). The excitation and detection situation inside the chamber is schematically shown in top-view in Fig. 3a and in side-view in Fig. 3b. The excitation laser beam is oriented 45° to the spray axis and sections one of the three spray streams. Along this beam waist of approximately 200 μm diameter, the Raman scattered light is collected spatially resolved at 90°. One example signal collection pathway from one of the resolved volume elements is indicated in yellow.

A length of 5.33 mm of the beam waist is imaged spatially and spectrally resolved onto the camera chip. To enhance the signal-to-noise-ratio (SNR), 800×200 superpixels were formed via two times two pixel hardware binning. For further SNR enhancement, eight of these superpixels were software binned along the spatial dimension, leading to finally 25×800 (spatial x spectral) super-pixels resolution. The sectional plane of the optical setup can be adjusted in terms of vertical position (height above injector h) and horizontal position along the excitation axis. When adjusting for a different height, the horizontal position has to be shifted accordingly to place the beam waist and detection position in the center of the spray stream.

At each set of conditions, 32 single measurements were carried out consecutively. For increase of data quality, the acquired images were later accumulated by software. An example signal distribution as acquired by the camera is shown in Fig. 4.

The spectral information S as a function of the Raman-shift $\bar{\nu}$ is shown on the horizontal axis, the depth axis resolves the spatial information. Two spatial positions marked in Fig. 3 as P_1 and P_2 are also marked in Fig. 4 for reference. Each spectrum S has been normalized to its respective maximum for better visibility, from which the ditch in the nitrogen peak line results between 3 and 4 mm. The spectrum at P_1 is from a position outside the spray. No ethanol is detected there, the nitrogen peak at 2330 cm^{-1} is visible. The spectrum at P_2 is inside the spray, the additional signal peaks between 2700 cm^{-1} and 3100 cm^{-1} emerge from the CH-vibration of ethanol, which at position P_2 (stream center) exceed the nitrogen peak intensity. The ones between 3200 cm^{-1} and 3800 cm^{-1} emerge from the OH-vibration of ethanol. According to,

$$\frac{n_{EtOH}}{n_{N_2}} = k \cdot \frac{I_{EtOH}}{I_{N_2}} \tag{1}$$

the ratio of the number of molecules of species ethanol (EtOH) n_{EtOH} and nitrogen (N$_2$) n_{N_2} is proportional to the ratio of the Raman signal intensities I_{EtOH} and I_{N_2} of the respective species in the mixture, with k beeing the proportionality constant. As Raman signal intensities for ethanol we consider the integral of the Raman spec-
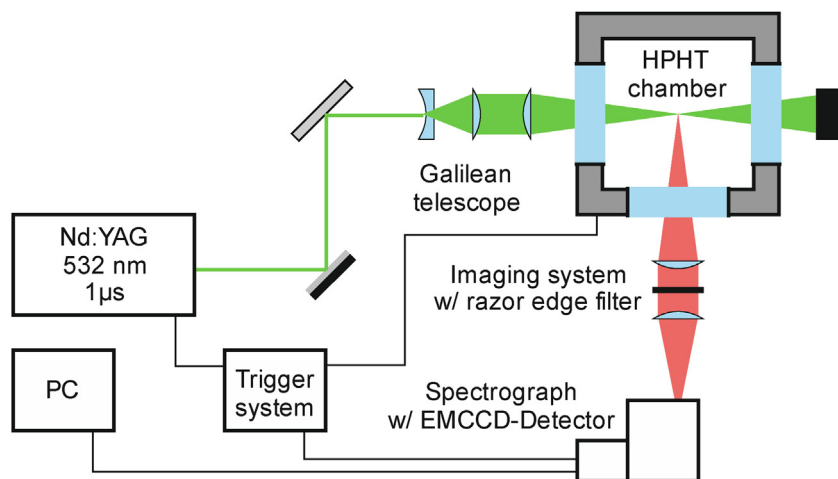
Fig. 2. Schematic overview of the setup around the high-pressure high-temperature (HPHT) chamber with optical pathways for excitation (green) and detection (red).
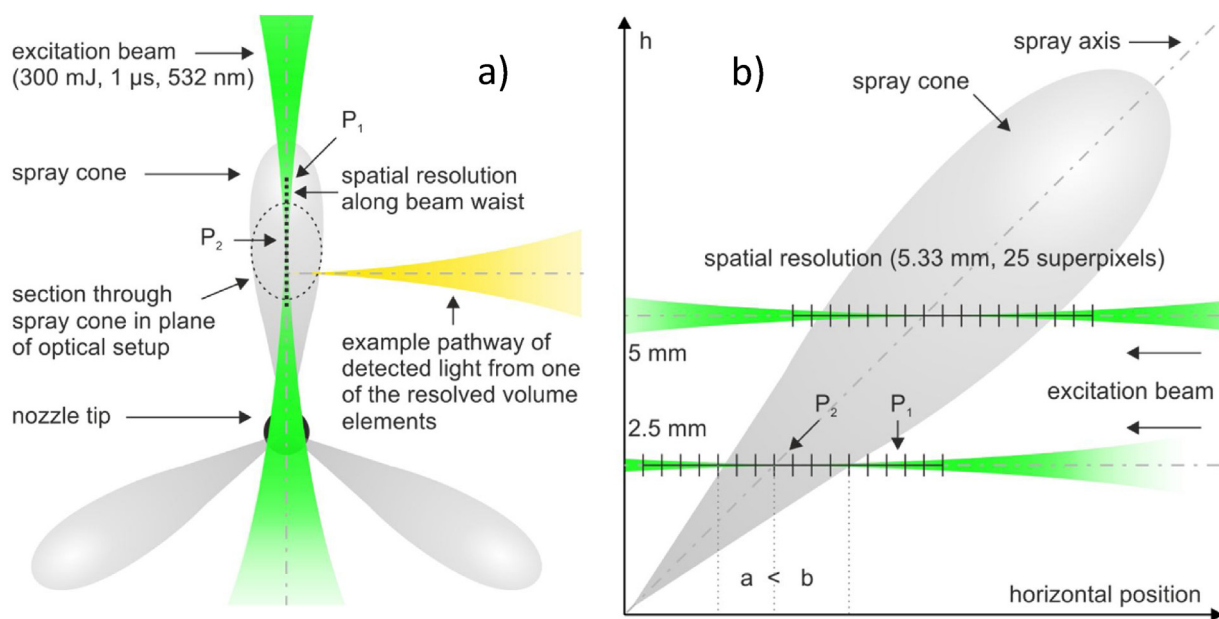

Fig. 3. Excitation and detection situation inside the chamber. The laser beam waist sections one of the three spray cones, detection in 90°, spatially resolved along the beam waist. a) Top view of the excitation and detection; b) Side view from detection side.
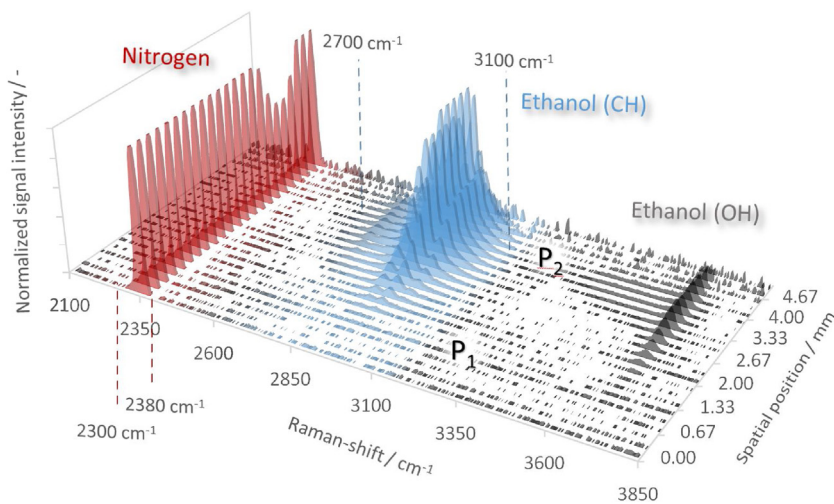

Fig. 4. Intensity distribution of Raman signals on camera chip. Spectral dimension on horizontal axis and spatial dimension on depth axis. Two spectra P_1 and P_2 are marked as outside and inside the spray. The nitrogen peak at about $2330\,cm^{-1}$ is highlighted in red, the CH-signal of ethanol at ~$2900\,cm^{-1}$ in blue. The OH-signal of ethanol is highlighted in grey.
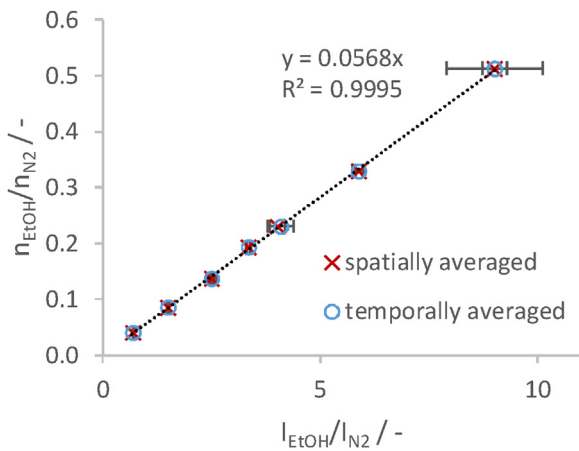
Fig. 5. Calibration results as set molar ratio of fuel to nitrogen over measured intensity ratio of fuel over nitrogen. Error bars quantify spatial or temporal standard deviation.

trum $I_{EtOH} = \int_{\bar{\nu}=2700cm^{-1}}^{\bar{\nu}=3100cm^{-1}} S d\bar{\nu}$ between $2700\,\mathrm{cm}^{-1}$ and $3100\,\mathrm{cm}^{-1}$. As Raman signal intensities for nitrogen we consider the integral of the Raman spectrum $I_{N_2} = \int_{\bar{\nu}=2300cm^{-1}}^{\bar{\nu}=2380cm^{-1}} S d\bar{\nu}$ between $2300\,\mathrm{cm}^{-1}$ and $2380\,\mathrm{cm}^{-1}$. The calibration factor k is obtained by calibration measurements, described in detail in the supporting information.

4. Evaluation procedures

4.1. Molar fuel fraction x_{EtOH}

Fig. 5 shows the linear relation between the molar ratios $\frac{n_{EtOH}}{n_{N_2}}$ and the measured intensity ratios $\frac{I_{EtOH}}{I_{N_2}}$ according to Eq. 1, where the slope of the best linear fit function is the desired calibration factor $k = 0.0568$. The data points shown in this figure were measured at various pressures (3 MPa - 5 MPa) and temperatures (573 K–673 K). Irrespectively of pressure and temperature, their correlation can be represented by one temperature and pressure insensitive linear fit. It is then possible to calculate the bulk molar ratio or the bulk molar fuel (ethanol:EtOH) fraction $x_{EtOH} = \frac{1}{1+\frac{n_{EtOH}}{n_{N_2}}}$ from spectra measured in the spray by applying Eq. 1. The intensity ratios given in Fig. 5 are averaged either spatially over the 25 spatial increments along the 5.33 mm long measurement length (detected beam waist) or temporally over 32 consecutively made measurements. The error bars represent in the case of spatial averaging the standard deviation of the 32 consecutively made measurements, while in the case of temporal averaging the error bars represent the standard deviation of the 25 spatially resolved increments along beam waist. For the calibration measurements, made at the largest ratio $\frac{n_{EtOH}}{n_{N_2}}$ the fed rather little amount of nitrogen has not been sufficient to generate a perfectly mixed ethanol/nitrogen-mixture in the calibration system. Therefore, the composition of the calibration mixture arriving in the calibration chamber varied in time, which is reflected by the larger error bar. For all other calibration points the composition of the calibration mixture was temporally constant resulting in a standard deviation of $\frac{I_{EtOH}}{I_{N_2}}$ of less than 2.8 % on average. Considering the slope of the calibration line, this standard deviation translates into a standard deviation of $\frac{n_{EtOH}}{n_{N_2}}$ of 0.0098.
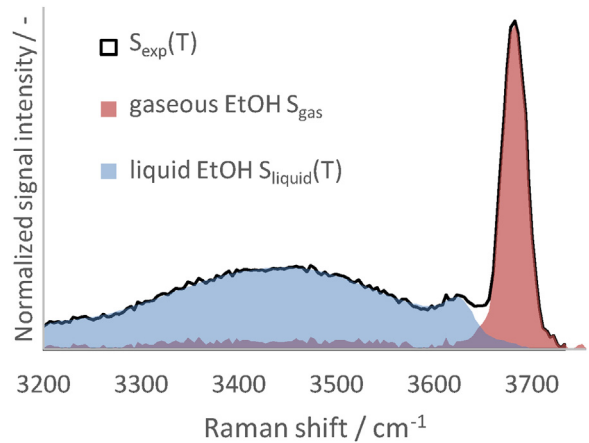

Fig. 6. Section of S_{exp} (T) between 3200 and 3800 cm^{-1} of example spectra of ethanol showing Raman OH-band. Spectrum of liquid ethanol S_{liquid} (T) at 403 K in blue, gaseous ethanol S_{gas} in red and an experimental spectrum S_{exp} (T) in black that contains signal contributions from liquid and gaseous ethanol simultaneously.

4.2. The fraction of ethanol contained in the liquid phase $x_{EtOH,liquid}$

The calculated molar fuel fraction x_{EtOH} does not hold information on whether the fluid is a single-phase liquid, a single-phase gas or in the single-phase supercritical state or a liquid/gas two-phase system. There might be either a homogeneous and comparably fuel-rich mixture of certain composition in the single-phase regime, or alternatively a two-phase mixture of identical composition but segregated into liquid domains of almost pure fuel surrounded by fuel-lean atmosphere (droplets surrounded by gas). The determination of the fluid state can be achieved by analyzing the Raman OH-band of ethanol, shown in Fig. 4. A zoomed view of this region of an example spectrum $S_{exp}(T)$ is shown in black in Fig. 6. $S_{exp}(T)$ contains contributions from liquid and gaseous ethanol. $S_{exp}(T)$ can be thus reproduced by the weighted summation of an experimental gaseous ethanol spectrum S_{gas}, which can be considered as not temperature sensitive [14], and a liquid spectrum $S_{liquid}(T)$, whose signature is sensitive to temperature [14]. Both are shown in Fig. 6 in red and blue respectively.

In order to deconstruct $S_{exp}(T)$ into the respective contributions $S_{liquid}(T)$ and S_{gas}, mathematical fitting of known spectra is applied in order to approximate the experimentally obtained spectrum S_{exp} [19]. Gas-phase ethanol spectra S_{gas} are available from the calibration measurements. The Raman spectra of ethanol in supercritical ethanol/nitrogen-mixtures are similar to the Raman spectra of gaseous ethanol, as it was shown before [13]. Liquid-phase ethanol spectra $S_{liquid}(T_{10K})$ are available from previous studies on the vapor/liquid-equilibria of this system for the here analyzed pressures between room temperature and the respective mixture critical temperature with a resolution of 10 K [13].

The sum of the gas-phase spectrum S_{gas} (fitted with respect to intensity by a factor a) and the liquid-phase spectrum $S_{liquid}(T_{10K})$ (fitted with respect to intensity by a factor b and with respect to band-shape by temperature T to pick the best fitting liquid spectrum from the database) are fitted to the measured spectrum $S_{exp}(T)$ according to

$$S_{exp}(T) = a \cdot S_{gas} + b \cdot S_{liquid}(T_{10K}) \qquad (2)$$

by least squares minimization of the residuals for Raman-shifts between $3400\,\mathrm{cm}^{-1}$ and $3750\,\mathrm{cm}^{-1}$. The restriction of the fitting spectral range to Raman shifts from $3400\,\mathrm{cm}^{-1}$ to $3750\,\mathrm{cm}^{-1}$ brings one decisive advantage. Especially at high temperatures, the liquid ethanol spectra $S_{liquid}(T_{10K})$ are rather insensitive to temperature

6   *T.C. Klima, A. Peter, S. Riess et al. / J. of Supercritical Fluids xxx (xxxx) xxx*

in this range. Therefore also in the event of having superheated ethanol present in the probe volume, the least squares minimization of Eq. 2 works using simply a high temperature spectrum of the liquid non-superheated) ethanol-rich phase. The final liquid phase ethanol spectrum is then obtained by

$$S_{liquid}(T) = S_{exp}(T) - a \cdot S_{gas} \tag{2}$$

subtracting the fitted gas phase spectrum S_{gas} from the experimental spectrum $S_{exp}(T)$. Following this method $S_{liquid}(T)$ is not restricted by the 10 K temperature resolution of the set of spectra available from previous vapor/liquid-equilibria measurements [13].

Summarizing, the separation of the contributions of ethanol in a liquid mixture and ethanol in a gaseous mixture to the spectrum of the overall mixture is solely based on the deconstruction of the Raman OH band of ethanol. For the calculation of the liquid ethanol fraction $x_{EtOH,liquid}$ (fraction of ethanol contained in the liquid phase)

$$x_{EtOH,liquid} = \frac{n_{EtOH,liquid}}{n_{EtOH,liquid} + n_{EtOH,gaseous}} = \left(1 + \frac{I_{EtOH,gaseous}}{I_{EtOH,liquid}} \cdot z\right)^{-1} \tag{3}$$

of the entire ethanol present in the observed volume, we consider the Raman CH-signal intensities $I_{EtOH,gaseous} = \int_{\bar{v}=2700cm^{-1}}^{\bar{v}=3100cm^{-1}} S_{gas}d\bar{v}$ and $I_{EtOH,liquid} = \int_{\bar{v}=2700cm^{-1}}^{\bar{v}=3100cm^{-1}} S_{liquid}d\bar{v}$ of the before separated gaseous S_{gas} and liquid ethanol $S_{liquid}(T)$ spectral contributions. In the respective equation (Eq. 3), the correction for the different electric excitation fields in the liquid phase and in the gaseous phase is incorporated via

$$z = \frac{\left(n_{refr., liquid} + 2\right)^4}{\left(n_{refr., gaseous} + 2\right)^4} \tag{4}$$

their indices of refraction $n_{refr., liquid}$ and $n_{refr., gaseous}$, respectively [20].

As the compositions of the liquid phase and of the vapor phase are not known (we only can quantify the overall mixture composition, which is an assembly of fluid elements in the liquid, the gaseous and supercritical state) we cannot apply the Lorentz-Lorenz relation for the estimation of the indices of refraction of both phases. Therefore, we take for the index of refraction of gaseous mixtures $n_{refr., gaseous} = 1$ and for liquid mixtures that one of pure ethanol at standard conditions $n_{refr., liquid} = 1.361$ [21]. A value of $z = 1.575$ results from these assumptions. It can be expected that at the here analyzed high pressures and high temperatures, the indices of refraction of the gaseous and the liquid mixture are larger than 1 and smaller than 1.361, respectively, as also the densities of the gaseous and liquid phase converge towards the critical point of the mixture. Consequently, the indices of refraction that we chose above, underestimate the liquid fraction in the mixture. Assuming equality of the indices of refraction of the liquid and the gaseous phases, a value of $z = 1$ results. Considering $z = 1$ instead of $z = 1.575$ would overestimate the liquid fuel fractions $x_{EtOH,liquid}$. Thus, the real fraction of ethanol contained in the liquid phase $x_{EtOH,liquid}$ is in between the values of $x_{EtOH,liquid,z=1.575}$ and $x_{EtOH,liquid,z=1}$ we obtain for the extremes of $z = 1.575$ and $= 1$.

4.3. The temperature of the liquid fraction T_{liquid}

The input data for the determination of the temperature of the liquid ethanol is the spectrum of the liquid ethanol $S_{liquid}(T)$ that we obtained in the previous step. We then use the integrated absolute difference spectrum (IADS) approach [21,22] for the tem-

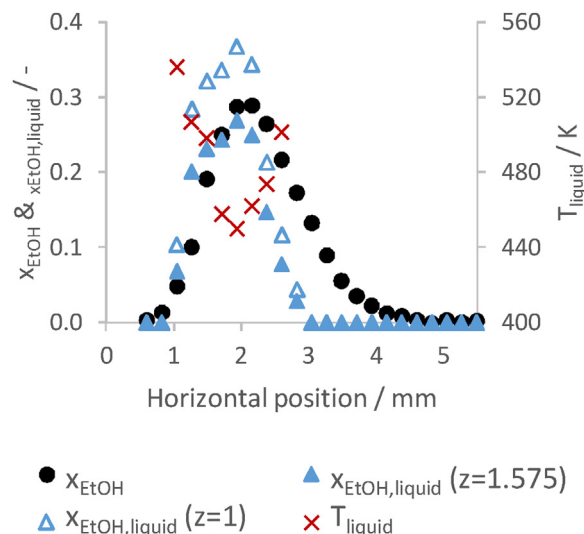**Fig. 7.** Ethanol fraction x_{EtOH}, fraction of ethanol in the liquid phase $x_{EtOH,liquid}$ and liquid phase temperature T_{liquid} along section of spray in 5 mm height. Ambient pressure is 6 MPa, ambient temperature is 923 K, 700 μs after start of injection. $x_{EtOH,liquid}$ as calculated for two different indices of refraction.

perature determination. From each liquid phase spectrum $S_{liquid}(T)$, the absolute difference to a reference spectrum of liquid ethanol measured at the respective ambient pressure p_a and at a injection temperature T_i of 363 K is calculated. Integrating the signal of this absolute difference spectrum yields an intensity that correlates with temperature. In [14], we showed that this correlation in the range of pressure and temperature conditions related to internal combustion devices is neither sensitive to pressure nor influenced by the presence of nitrogen in the liquid mixture. Furthermore, we extended the IADS function to temperatures above the mixture critical temperature and thus were able to estimate the temperature of superheated ethanol. As it is not possible to calibrate at superheated conditions, simply because they are in the thermodynamic region of meta- or instability, we cannot detail on the quality of the extrapolated superheated temperatures and just provide them as estimation. Nonetheless, this method, simply based on the determined temperatures, enables the differentiation between a superheated liquid and a non-superheated liquid phase.

5. Results

With the described evaluation methods, it is possible to derive all at once, the molar ethanol fraction x_{EtOH} in the mixture, the fraction of ethanol contained in the liquid phase $x_{EtOH,liquid}$ of the mixture (liquid ethanol fraction) and the temperature T_{liquid} of that liquid fraction from the spectra measured along a line in a certain height above the injector nozzle exit. Fig. 7 shows this combined and simultaneously acquired information spatially resolved (horizontal position in Fig. 7) along the beam waist. The shown data were measured at injection conditions of $p_a = 6\,MPa$, $T_a = 923\,K$, and 700 μs after the start of injection, when the spray stream is stationary (no more effect of the needle opening behavior). The height probed is 5 mm above the injector nozzle. Due to the elevation angle of 45° the penetration depth of the center of the stream is 7.1 mm. Both variants for the correction of the index of refraction given as in Eq.(3) are shown, either for $z = 1.575$ or $z = 1$. Since the real index of refraction of the liquid phase during the measurements is assumed to be somewhere within this range, the real liquid fraction is also bound to be somewhere between the data points shown here.

All spatially and temporally resolved data for x_{EtOH}, $x_{EtOH,liquid}$ and T_{liquid} for all investigated operational conditions can be found in [22].

In Fig. 7, the laser beam penetrates the spray steam from right to left. The horizontal position of 2 mm can be assumed to be the spray axis, as along the spray axis the largest ethanol fractions x_{EtOH} are expected. The distribution of the ethanol molar fraction x_{EtOH} and the fractions of ethanol in the liquid phase $x_{EtOH,liquid}$ are asymmetric, resulting from the sectioning of the spray stream under 45° angle with respect to the spray's axis. Two consequences result: Firstly, horizontal positions left of the spray axis feature a shorter penetration depth than those right of the spray axis. Secondly, the portion of the spray stream left of the spray axis is smaller than it is right of the spray stream center. Thus, x_{EtOH} on the left side of the maximum increases steeper than it decreases on the right side of the maximum. Due to the shorter penetration depth left of the spray stream center and thus due to less time available for heat and mass transfer between the injected ethanol and the ambient nitrogen, the distribution of the ethanol fraction in the liquid phase $x_{EtOH,liquid}$ shows larger values on the left side of the spray stream center than on the right side. The fuel on this side has not been exposed to the ambient gas as long as on the right side, leading to shorter heating and less transfer from the liquid phase to the gaseous or supercritical phase.

The lowest liquid phase temperature T_{liquid} is found in the position of the highest $x_{EtOH,liquid}$, with increasing temperature towards the flanks of the spray with decreasing liquid fraction. On the left hand side of the spray, with respect to the figure, a liquid phase temperature above the mixture critical temperature of ethanol is found, indicating dense volumes with large fractions of ethanol in a superheated state.

In order to ensure reliable evaluation, $x_{EtOH,liquid}$ was only calculated when $x_{EtOH} > 0.1$, and T_{liquid} only when $x_{EtOH,liquid} > 0.05$. The data quality also depends on the penetration depth of the laser beam through the spray stream and thus onto the horizontal position. The laser beam is scattered from liquid/gas interfaces and refracted from gradients of the index of refraction when penetrating the spray stream, resulting in degrading signal-to-noise with depth of penetration through the spray stream. Data for x_{EtOH}, $x_{EtOH,liquid}$ or T_{liquid} calculated for horizontal positons between 0 and 1 are thus not reliable and are therefore neglected in the following.

Fig. 8 shows for two operational conditions, 8 MPa / 573 K (top) and 8 MPa / 923 K (bottom), the measured liquid phase temperature T_{liquid} over the measured ethanol molar fraction x_{EtOH} as data points for different measurement heigts above the injector nozzle. The boiling (BPC) ad dew (BPC) point curves are taken again from our previous investigations [13].

Most of the data points occupy the region left of the dew point line in the region that thermodynamically is assigned to a single gaseous phase. But in the sections above it was described that we only can derive a liquid ethanol temperature T_{liquid} from locations for which we also were able to detect a liquid ethanol fraction $x_{EtOH,liquid} > 0.05$. This conflict is justified in the following. The probed volume that corresponds to one measurement point is approximately 200 μm in depth (diameter of laser beam waist) times 200 μm in height (diameter of laser beam waist) times 213 μm (incremental resolution along the laser beam waist). If within this volume liquid and gaseous mixture ligaments coexist, x_{EtOH} will just provide the composition averaged over the ligaments contained in the entire volume. If the amount of matter in the ethanol-lean gaseous ligaments significantly exceeds the amount of matter in the ethanol-rich liquid ligaments, the overall measured x_{EtOH} will be dominated by the ethanol-lean gaseous phase. Therefore, the data points in Fig. 8 occupy the single phase gaseous region, though for all of them we also detected ethanol in a liquid mixture. The same consequence arises from averaging 32 single-shot
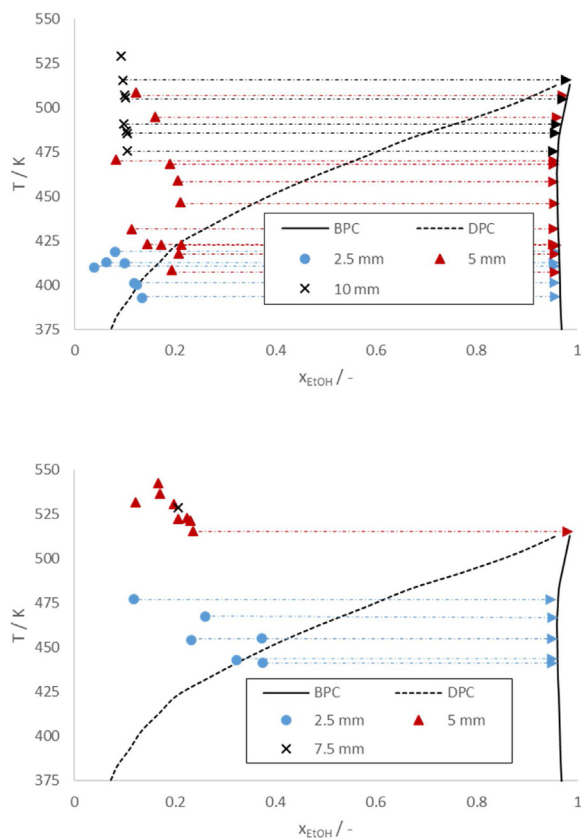

Fig. 8. Liquid phase temperatures T_{liquid} over the measured ethanol molar fraction x_{EtOH} for two example operational conditions 8 MPa / 573 K (top) and 8 MPa / 923 K (bottom). The isothermal projection of the data points for which liquid ligaments were detected to the single phase liquid region is indicated by the arrows.

measurements to mean data points. If at a certain measurement location the fluid phase (liquid or gaseous) fluctuates from shot to shot, x_{EtOH} after averaging the spectra also provides just an average of the various 32 measurements from which some correspond to liquid and others to gaseous mixtures. The same conflict would occur for all other measurement techniques that are not able to resolve or detect phase heterogeneities within the probed volume.

The advantage of the here presented measurement technique is that we are able to detect the existence of liquid ligaments that are smaller than the spatial resolution of the measurement setup. This is possible because of the analysis of $x_{EtOH,liquid}$. We assume that the composition of the liquid mixture ligaments can only be between the one of pure ethanol ($x_{EtOH} = 1$) and the saturated liquid phase ($x_{EtOH} = x_{EtOH,boiling}$, composition along the boiling point line in Fig. 8). Therefore, we can project all the data points in Fig. 8 that occupy the single-phase gaseous region into the single phase liquid mixture region, as indicated by the arrows in Fig. 8.

The projected data points then approximate the composition and the temperature of the liquid mixture ligaments only. The data points exceeding the mixture critical temperature (MCT) cannot be moved isothermally across the boiling point line (not existing above the MCT). Therefore we did not project them.

Considering all analyzed operational conditions, only for the highest set temperature of 923 K we detected few liquid phase temperatures exceeding the MCT (compare Fig. 8). The operational condition 8 MPa/923 K (highest pressure at highest temperature) is the only one for which we were able to detect a significant number of liquid phase temperatures exceeding the MCT. For ambient temperatures below 923 K we did not detect any liquid phase temperature above the MCT. Hence, we conclude that superheated
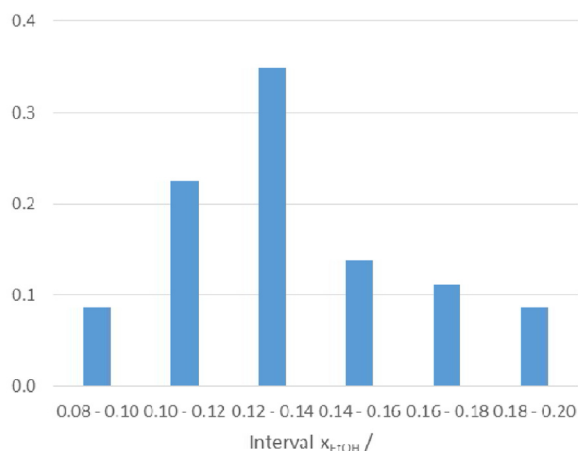
Fig. 9. Probability density presentation of the mixture compositions x_{EtOH} measured for all data points for which the simultaneously detected $x_{EtOH,liquid}$ was between 0 and 0.05 (no liquid phase existing).

liquid mixtures (T_{liquid} >MCT) exist at the highest set ambient temperatures of 923 K, though also the other ambient temperatures were all above the $T_a > MCT$ and therefore could have resulted potentially - but did not - in liquid phase mixture temperatures above the MCP.

Fig. 9 summarizes all measured mixture compositions x_{EtOH} for which we did not detect the existence of a liquid fraction, i.e. for which the fraction of ethanol in a liquid phase was between the interval $0 \le x_{EtOH,liquid} \le 0.05$ in a probability density presentation.

Fig. 9 reveals that all mixture fractions x_{EtOH} measured for mixtures that did not contain liquid mixture ligaments are below $x_{EtOH} = 0.2$. This implies that in all these single-phase mixtures ethanol is highly diluted with nitrogen. We did not find a single data point representing a single-phase mixture that did not contain liquid ligaments ($0 \le x_{EtOH,liquid} \le 0.05$) but featuring at the same time fractions of ethanol above $x_{EtOH} > 0.2$.

6. Conclusion

Summarizing the interpretations related to Figs. 8 and 9, we can conclude that we were able to detect for ambient temperatures $T_a < 923 K$

- either mixtures that contained liquid ligaments which were not superheated
- or mixtures that did not contain liquid ligaments but contained less than 20 mol-% ethanol.

For ambient temperatures $T_a = 923 K$ we were able to detect

- either non-superheated together with few superheated ligaments, with an increasing occurance of superheated ligaments with increasing pressure (volume specific enthalpy).
- or again mixtures that did not contain liquid ligaments but contained less than 20 mol-% ethanol.

We never detected mixtures that did not contain liquid ligaments but with ethanol fractions between $0.2 < x_{EtOH} < 1$. We therefore conclude that for $T_a < 923 K$ the mixing path that we in Fig. 1 referred to as single-phase mixing process effectively does not take place. In other words, the mixing process for $T_a < 923 K$ is governed by the two-phase mixing path. The data show that merely setting the ambient temperature exceeding the critical temperature of the fuel is not sufficient to obtain a purely single-phase mixing process or a "supercritical spray".

At the highest ambient temperature $T_a = 923 K$, and especially at the highest ambient pressure of $p_a = 8 MPa$, we found mixtures that contained liquid ligaments with superheated liquid phase temperatures. With increasing depth of penetration, the number of measured liquid phase temperatures above the MCT increased. According to the mixing paths shown in Fig. 1 the existence of liquid-like ethanol-rich ligaments with temperatures above the MCT is essential for the existence of a single-phase mixing process. Only then, the mixing path can circumvent the two-phase region. We therefore conclude that, with sufficient ambient enthalpy and residence time, liquid structures can be sufficiently heated to achieve single-phase mixing as shown in Fig. 1. Even though the ethanol/nitrogen mixtures do not become "really supercritical", as for this much higher pressures and temperatures would be required, the mixture formation in the Tx-diagram is continuous then, i.e. the phase boundary typically limiting the mass transfer from fuel-rich, liquid-like volumes to the fuel-lean vapor phase, is not present here.

These observations were made possible by separating the signals contributions of the fuel ethanol originating from the liquid and from the gaseous phases from each other. We want to emphasize that the temperature evaluation method we introduce here is based only on the liquid fraction of the fuel. No information about the temperature of the fuel-poor ambient phase that surrounds the liquid domains can be made. But a careful analysis of the shape of the Q-branch signal of nitrogen can most probably make the temperature of the non-liquid-phase accessible. Measurement techniques that cannot differentiate between the signal contributions from either the liquid or the gaseous phase most probably do not have the capacity to identify the existence of a liquid phase. This was demonstrated by analyzing the ethanol molar fractions we evaluated from experimentally acquired spectra that had not been separated before into their liquid and gaseous shares. The described technique and data evaluation methods are applicable to similar processes, provided the fuel develops hydrogen bonds.

Declaration of Competing Interest

The authors declare that they have no known competing financial interests or personal relationships that could have appeared to influence the work reported in this paper.

Acknowledgements

References

[1] G. Castiglioni, J. Bellan, On models for predicting thermodynamic regimes in high-pressure turbulent mixing and combustion of multispecies mixtures, J. Fluid Mech. 843 (2018) 536–574, http://dx.doi.org/10.1017/jfm.2018.159.
[2] G. Lamanna, C. Steinhausen, B. Weigand, A. Preusche, B. Bork, A. Dreizler, et al., On the importance of non-equilibrium models for describing the coupling of heat and mass transfer at high pressure, Int. Commun. Heat Mass Transf. 98 (2018) 49–58, http://dx.doi.org/10.1016/j.icheatmasstransfer.2018.07.012.
[3] S. Baab, C. Steinhausen, G. Lamanna, B. Weigand, F.J. Förster, A quantitative speed of sound database for multi-component jet mixing at high pressure, Fuel 233 (2018) 918–925, http://dx.doi.org/10.1016/j.fuel.2017.12.080.
[4] L. Qiu, R.D. Reitz, An investigation of thermodynamic states during high-pressure fuel injection using equilibrium thermodynamics, Int. J.

Multiph. Flow 72 (2015) 24–38, http://dx.doi.org/10.1016/j.ijmultiphaseflow.2015.01.011.

[5] Z. Falgout, M. Rahm, D. Sedarsky, M. Linne, Gas/fuel jet interfaces under high pressures and temperatures, Fuel 168 (2016) 14–21, http://dx.doi.org/10.1016/j.fuel.2015.11.061.

[6] R.N. Dahms, J.C. Oefelein, Liquid jet breakup regimes at supercritical pressures, Combust. Flame 162 (10) (2015) 3648–3657, http://dx.doi.org/10.1016/j.combustflame.2015.07.004.

[7] C. Crua, J. Manin, L.M. Pickett, On the transcritical mixing of fuels at diesel engine conditions, Fuel 208 (2017) 535–548, http://dx.doi.org/10.1016/j.fuel.2017.06.091.

[8] J. Manin, M. Bardi, L.M. Pickett, R.N. Dahms, J.C. Oefelein, Microscopic investigation of the atomization and mixing processes of diesel sprays injected into high pressure and temperature environments, Fuel 134 (2014) 531–543, http://dx.doi.org/10.1016/j.fuel.2014.05.060.

[9] R.N. Dahms, J.C. Oefelein, On the transition between two-phase and single-phase interface dynamics in multicomponent fluids at supercritical pressures, Phys. Fluids 25 (9) (2013) 92103, http://dx.doi.org/10.1063/1.4820346.

[10] R.N. Dahms, Understanding the breakdown of classic two-phase theory and spray atomization at engine-relevant conditions, Phys. Fluids 28 (4) (2016) 42108, http://dx.doi.org/10.1063/1.4946000.

[11] L. Qiu, R.D. Reitz, Simulation of supercritical fuel injection with condensation, Int. J. Heat Mass Transf. 79 (2014) 1070–1086, http://dx.doi.org/10.1016/j.ijheatmasstransfer.2014.08.081.

[12] S. Riess, L. Weiss, A. Peter, J. Rezaei, M. Wensing, Air entrainment and mixture distribution in Diesel sprays investigated by optical measurement techniques, Int. J. Engine Res. 19 (1) (2018) 120–133, http://dx.doi.org/10.1177/1468087417742527.

[13] T.C. Klima, A.S. Braeuer, Vapor-liquid-equilibria of fuel-nitrogen systems at engine-like conditions measured with Raman spectroscopy in micro capillaries, Fuel 238 (2019) 312–319, http://dx.doi.org/10.1016/j.fuel.2018.10.108.

[14] T.C. Klima, A.S. Braeuer, Raman thermometry in water, ethanol and ethanol/nitrogen-mixtures from ambient to critical conditions, Anal. Chem. (2018), http://dx.doi.org/10.1021/acs.analchem.8b04382.

[15] J. Egermann, M. Taschek, A. Leipertz, Spray/wall interaction influences on the diesel engine mixture formation process investigated by spontaneous Raman scattering, Proc. Combust. Inst. 29 (1) (2002) 617–623, http://dx.doi.org/10.1016/S1540-7489(02)80079-7.

[16] R.F. Hankel, A. Günther, K.-E. Wirth, A. Leipertz, A. Braeuer, Liquid phase temperature determination in dense water sprays using linear Raman scattering, Opt. Express 22 (7) (2014) 7962–7971, http://dx.doi.org/10.1364/OE.22.007962.

[17] T. Müller, G. Grünefeld, V. Beushausen, High-precision measurement of the temperature of methanol and ethanol droplets using spontaneous Raman scattering, Appl. Phys. B 70 (1) (2000) 155–158, http://dx.doi.org/10.1007/s003400050024.

[18] D. Bassing, A.S. Braeuer, The lag between micro- and macro-mixing in compressed fluid flows, Chem. Eng. Sci. 163 (2017) 105–113, http://dx.doi.org/10.1016/j.ces.2017.01.034.

[19] E. Kriesten, F. Alsmeyer, A. Bardow, W. Marquardt, Fully automated indirect hard modeling of mixture spectra, Chemom. Intell. Lab. Syst. 91 (2) (2008) 181–193, http://dx.doi.org/10.1016/j.chemolab.2007.11.004.

[20] J.R. Nestor, E.R. Lippincott, The effect of the internal field on Raman scattering cross sections, J. Raman Spectrosc. 1 (3) (1973) 305–318, http://dx.doi.org/10.1002/jrs.1250010309.

[21] D.R. Lide (Ed.), CRC Handbook of Chemistry and Physics: A Ready-Reference Book of Chemical and Physical Data, 86th ed., CRC Press, Boca Raton, 2005.

[22] T.C. Klima, A. Peter, S. Riess, M. Wensing, A.S. Braeuer, Mixture Composition, Liquid-Phase Fraction and -Temperature in Transcritical Sprays, Mendeley Data, 2019, http://dx.doi.org/10.17632/2v3k4s27r9.1 (v1).